JGR Oceans

RESEARCH ARTICLE
10.1029/2019JC015430

Source Regions of Infragravity Waves Recorded at the Bottom of the Equatorial Atlantic Ocean, Using OBS of the PI-LAB Experiment

P. Bogiatzis[1], A. Karamitrou[2,3], J. Ward Neale[4], N. Harmon[1], C. A. Rychert[1], and M. Srokosz[4]

[1]Ocean and Earth Science, National Oceanography Centre Southampton, University of Southampton, Southampton, UK, [2]Department of Geophysics, Aristotle University of Thessaloniki, Thessaloniki, Greece, [3]Now at Archaeology, University of Southampton, Southampton, UK, [4]National Oceanography Centre, Southampton, UK

Key Points:
- We developed a new global back-projection method of noise cross-correlation that minimizes array geometry effects using adaptive weighting
- The most energetic sources of infragravity waves we observe are located at the Atlantic coasts of Africa, Antarctica, and South America
- We find indications of infragravity waves propagating with little attenuation, long distances through sea ice, reflecting off Antarctica

Supporting Information:
- Supporting Information S1

Correspondence to:
P. Bogiatzis,
p.bogiatzis@soton.ac.uk

Citation:
Bogiatzis, P., Karamitrou, A., Ward Neale, J., Harmon, N., Rychert, C. A., & Srokosz, M. (2020). Source regions of infragravity waves recorded at the bottom of the equatorial Atlantic Ocean, using OBS of the PI-LAB experiment. *Journal of Geophysical Research: Oceans*, *125*, e2019JC015430. https://doi.org/10.1029/2019JC015430

Received 28 JUN 2019
Accepted 12 MAY 2020
Accepted article online 19 MAY 2020

© 2020. The Authors.
This is an open access article under the terms of the Creative Commons Attribution License, which permits use, distribution and reproduction in any medium, provided the original work is properly cited.

Abstract Infragravity waves are generated along coasts, and some small fraction of their energy escapes to the open oceans and propagates with little attenuation. Due to the scarcity of deep-ocean observations of these waves, the mechanism and the extent of the infragravity waves energy leakage from the coasts remains poorly understood. Understanding the generation and pathways of infragravity wave energy is important among others for understanding the breakup of ice-shelves and the contamination of high-resolution satellite radar altimetry measurements of sea level. We examine data from 37 differential pressure gauges of Ocean Bottom Seismometers (OBS) near the equatorial mid-Atlantic ridge, deployed during the Passive Imaging of the Lithosphere-Asthenosphere Boundary (PI-LAB) experiment. We use the beamforming technique to investigate the incoming directions of infragravity waves. Next, we develop a graph-theory-based global back-projection method of noise cross-correlation function envelopes, which minimizes the effects of array geometry using an adaptive weighting scheme. This approach allows us to locate the sources of the infragravity energy. We assess our observations by comparing to a global model of infragravity wave heights. Our results reveal strong coherent energy from sources and/or reflected phases at the west coast of Africa and some sources from South America. These energy sources are in good agreement with the global infragravity wave model. In addition, we also observe infragravity waves arriving from North America during specific events that mostly occur during October–February 2016. Finally, we find indications of waves that propagate with little attenuation, long distances through sea ice, reflecting off Antarctica.

Plain Language Summary Infragravity waves are oceanic surface waves with periods between 30 and 300 s and wavelengths up to tens of kilometers. They are generated along coasts; however, a small fraction of the energy escapes to the open ocean and travels with little attenuation over transoceanic distances. They play a significant role in phenomena such as seiches, coastal barrier breaching, and the break-up of ice-shelves. Therefore, it is important to determine their sources, how they propagate through the ocean and their interactions with the coasts. To shed light on these questions, we examine pressure data recorded at an array of ocean bottom instruments deployed beneath the equatorial Atlantic Ocean. We use array techniques to turn the ambient infragravity energy noise into useful signal, allowing the determination of the incoming directions and the sources of these waves. Our results reveal strong infragravity wave sources at the Atlantic coasts of Africa and South America. We also observe significant energy arriving from Antarctica possibly due to waves generated elsewhere reflecting off Antarctic coasts.

1. Introduction

Infragravity waves are oceanic surface gravity waves with typical frequencies between 0.003 and 0.03 Hz, and wavelengths of the order of several kilometers. They are generated from nonlinear difference interactions of the higher frequency wind waves and swells and are more energetic near coastlines (Ardhuin et al., 2014; Biesel, 1952; Herbers et al., 1994; Herbers, Elgar, & Guza, 1995; Smit et al., 2018; Webb et al., 1991). It has also been suggested (Symonds et al., 1982) that they can be generated by a time-varying breakpoint with standing waves shoreward of the breakpoint and outgoing progressive infragravity waves propagating offshore of the breakpoint. Although such nonlinear wave-wave interactions responsible for the excitation of infragravity wave motions exist both in deep water and the coasts, they experience resonant

interactions only near the coast, where they produce significant forced response (e.g., Ardhuin et al., 2014; Herbers, Elgar, Guza, & O'Reilly, 1995; Webb et al., 1991). This is more evident in high-energy coasts with narrow continental shelves (e.g. Smit et al., 2018).

Infragravity waves are important for a wide variety of phenomena including coastal flooding, seismic noise, and understanding sea ice thickness variations. They can create seiches at harbors and coastal regions and contribute to flooding phenomena and coastal barrier breaching when the amplitudes of the waves increase in shallow water (e.g., Aucan & Ardhuin, 2013; Okihiro & Guza, 1996; Reniers et al., 2010; Sheremet et al., 2014). Even when their amplitudes are small, they can play an important role in the breakup of ice shelves in polar regions (e.g., Bromirski et al., 2010, 2015, 2017; Dumont et al., 2011; Kohout et al., 2014). It has also been shown that infragravity waves phase dispersion is sensitive to the sea ice thickness; and therefore, they can be used for measuring the thinning of Arctic sea ice, which has been proven to be a challenging task (Wadhams & Doble, 2009). Infragravity waves are also responsible for the Earth's hum (e.g., Ardhuin et al., 2015; Rhie & Romanowicz, 2006; Webb, 2007, 2008). It has been suggested that they are a potential source of the acoustic gravity waves in the atmosphere (e.g., Godin et al., 2015; Zabotin et al., 2016), and thus play an important role in the coupling between motions in the ocean, ice, atmosphere, and the solid Earth. Finally, from an observational perspective, it has been shown (Ardhuin et al., 2014; Aucan & Ardhuin, 2013) that the infragravity waves can introduce errors in the next-generation, high-resolution satellite sea-level altimetry measurements that aim to detect mesoscale (10–200 km) and submesoscale (1–10 km) features, adding to the necessity of their accurate modeling and data-driven investigation. Therefore, obtaining better observational constraints on infragravity waves has an impact over a broad range of fields.

Most of the infragravity wave energy refracts along the shorelines and propagates within some hundreds of meters from the shore in the form of edge waves, observed in shallow coastal waters (Herbers, Elgar, & Guza, 1995; Herbers, Elgar, Guza, & O'Reilly, 1995; Munk, 1949; Munk et al., 1964; Tucker, 1950) and beneath the surface of sea ice (Mahoney et al., 2016). It is estimated that less than 1% of the energy of infragravity waves leaks onto the open ocean (Webb et al., 1991) and travels transoceanic distances with negligible attenuation (e.g., Godin et al., 2013), reaching the other side of the oceanic basin (e.g., Harmon et al., 2012; Tonegawa et al., 2018). Due to insufficient high-resolution observations in deep ocean basins, the mechanism, dynamics, and energy levels of the infragravity waves energy leakage from the coasts onto the deep ocean is poorly understood (e.g., Aucan & Ardhuin, 2013). It has been suggested that the local bathymetry and topography along shore may be an important factor (Uchiyama & McWilliams, 2008). However, recent numerical models that account for the nearshore under the assumption of locally straight shoreline, produce relatively good agreement with measured infragravity amplitudes (Ardhuin et al., 2014), posing indirectly an upper limit to the contribution of small-scale morphology.

In this work, we investigate year-long, deep-ocean pressure recordings from Ocean Bottom Seismometers (OBS) at the equatorial mid-Atlantic ridge. The aim of this study is to determine the directions of the infragravity energy that reaches the mid-Atlantic Ocean basin, and to locate the sources of the infragravity waves leakage at the surrounding coastlines. We calculate the noise cross-correlations between pairs of the stations, and then we examine the incoming directions by means of the beamforming technique. Next, we develop a global back-projection method (e.g., Harmon et al., 2012; Kiser & Ishii, 2017; Neale et al., 2015) that uses the shortest path method to calculate the ray paths at a global scale. To mitigate artifacts due to the elongated array geometry (e.g., Kiser & Ishii, 2017; Neale et al., 2015), we introduce a two-stage, adaptive weighting back-projection scheme, which optimizes the response of the array without excluding any stations. Finally, we back-project the energy of the infragravity waves to determine their possible origins.

2. Data

We use ocean bottom pressure recordings from differential pressure gauges deployed as part of the Passive Imaging of the Lithosphere-Asthenosphere Boundary (PI-LAB) experiment at the equatorial Mid-Atlantic Ridge from March of 2016 to March of 2017. More specifically, we process data from 37 stations with depths that vary from 2,905 to 5,205 m (Figure 1). The pressure timeseries from each station are down sampled to 1 Hz, and the amplitudes are normalized with the maximum of the envelope of the waveform to reduce the

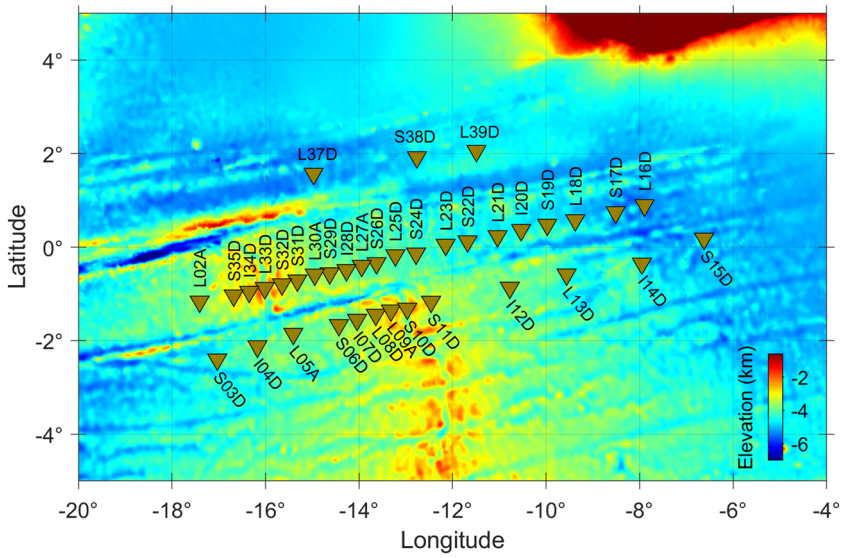

Figure 1. Map showing the OBS stations (inverted triangles) of the PI-LAB experiment and the bathymetry (Amante & Eakins, 2009). Text indicates the code names of the stations.

effects of earthquakes in the data and differences in the calibration of the sensors. Next, we calculate cross-correlograms for all possible pairs of the stations and for each day of the deployment. Finally, for each station pair, the stack of up to 361 days of the cross-correlations is generated, yielding its noise cross-correlation function (NCF). After visual inspection of the envelopes of the stack of the NCFs, station pairs with either poor signal-to-noise ratio and/or instrument problems are discarded, yielding to a total of 202 NCFs (Figure 2) used for the back-projection method described later. More advanced techniques for data selection (e.g., Valentine & Woodhouse, 2010) are not applicable due to the limited size of this data set. The lag time for these calculations is ±10,800 s corresponding to a 6-hr window.

Through the procedure of amplitude normalization and stacking described above, we effectively study the coherent wave energy that propagates across each station pair. In other words, we are sensitive to the relative amount of coherent waves through time in the stack, but not necessarily the amplitude of wave events. Asymmetry in the amplitude between positive and negative lag in single NCFs suggests analogous asymmetry in the amount of coherent energy that propagates in the corresponding directions.

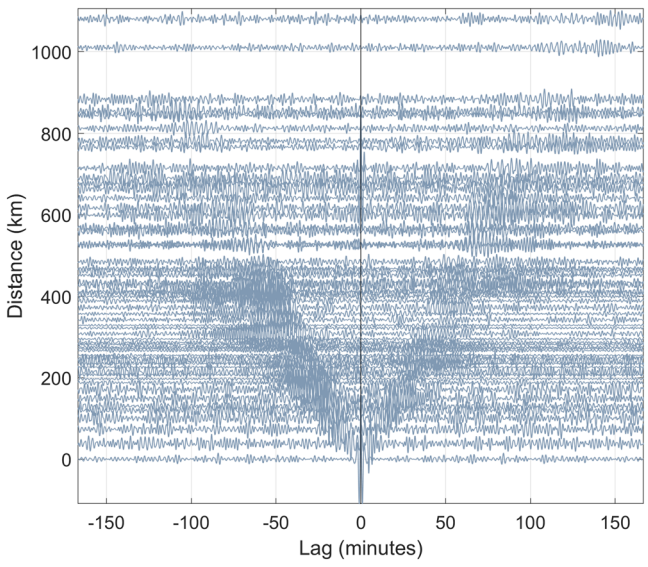

Figure 2. Stack of 361 days of noise cross-correlation functions, bandpass filtered between 100 and 200 s.

3. Methods

We present the two array techniques that were used in this work to detect the direction of the transient energy that propagates across the PI-LAB array and the potential sources of this energy, namely, incoherent beamforming and back-projection.

3.1. Incoherent Beamforming

Beamforming is a spatial filtering technique that is used to investigate the direction of energy propagation across an array, as a function of slowness (reciprocal of velocity) and azimuth, by assuming a plane wave propagating through the array. The incoherent beamforming technique differs from the conventional beamforming because it utilizes the envelope of the waveform, instead of the waveform itself. Thus, the incoherent beamforming technique has only positive values, since incoherent arrivals do not cancel to zero. This results in generally noisier beamformers; however, it is more effective for the detection of highly scattered arrivals (e.g., Ringdal et al., 1975).

The lag time of the envelope corresponds to the wave-group travel-time between two stations. Therefore, the beam expresses the value of the cross-correlation envelope (C_n) at the expected lag-time for a group slowness s and azimuth θ.

$$B\left(f_p, s, \theta\right) = \sum_{n=1}^{N} \left\langle C_n\left(f_p, T_n(s,\theta)\right)\right\rangle, \tag{1}$$

where $\langle\cdot\rangle$ denotes the envelope of the signal and C_n is the cross correlation for the station pair n. T_n, is the expected group travel time between the stations in the station pair n, and it is calculated for a synthetic plane wave as,

$$T_n(s,\theta) = s \cdot d_n \cdot \cos(u - \varphi_n), \tag{2}$$

where d_n and φ_n are the distance and the azimuth, respectively, between the stations of the station pair n, for plane wave with azimuth u. To center the angular frequency ω_c, a Gaussian band-pass filter, $f = \exp\left(-\frac{a(\omega-\omega_c)^2}{\omega^2}\right)$, is applied, with $a = 100\sqrt{d_n \cdot 10^{-3}}$, where ω is the angular frequency.

3.2. Back-Projection

The back-projection method has been widely used to image the rupture process of large earthquakes (e.g., Ishii et al., 2005; Kiser & Ishii, 2017), and for the determination of the infragravity wave sources (e.g., Harmon et al., 2012; Neale et al., 2015; Tonegawa et al., 2018). It provides information of a relative nature, such as the location of the recorded coherent energy, relative to the array. Furthermore, it should be noted that the back-projected quantities are NCFs between differential pressure gauges of which the amplitude information has been removed through the normalization process that is described in section 2. Therefore, the results are solely dependent upon the coherence of the phase of the signal and cannot be directly related with absolute measures such as the wave amplitude or the magnitude of an event. In this work, the back-projection method is applied to locate coherent sources of infragravity waves, using NCFs.

More specifically, the envelope of the stack of the NCFs is back-projected onto an orthogonal grid of points at the surface of the Earth. The grid is created using the JIGSAW-GEO software (Engwirda, 2017), producing a uniform, orthogonal mesh with spatial resolution of 150 km. Grid points that correspond to continental regions are removed. Following Harmon et al. (2012) and Neale et al. (2015), the back-projected source density P, for the center angular frequency ω, is calculated as

$$P(\varphi,\theta,\omega) = \sum_{n=\{i,j\}} W_n \cdot \left\langle C_n\left(t_i(\varphi,\theta,\omega) - t_j(\varphi,\theta,\omega)\right)\right\rangle, \tag{3}$$

where W_n are weights that mitigate the array geometry effects, described below, and t_i the group velocity travel times from the station indicated by the subscript to the point of the Earth's surface with coordinates (*latitude*, *longitude*) = (φ, θ). It should be noted that both the negative and positive lag-times are included in the back-projection. The travel times are calculated based on the theoretical group velocity, U, using the dispersion relationship for surface gravity waves as a function of ω and the water column depth h (e.g., Webb et al., 1991) as

$$\omega = \sqrt{k \cdot g \cdot \tanh(k \cdot h)}, \tag{4}$$

$$|U| = \frac{\partial\omega}{\partial k}, \tag{5}$$

where $g = 9.81\frac{m}{s^2}$ is the acceleration due to gravity, and k is the wavenumber. For determining h, the bathymetry data from Amante and Eakins (2009) with spatial resolution of one arc minute are used. The bathymetry data are interpolated to the grid points of a mesh similar to that used for the back-projection, but with spatial resolution that increases sinusoidally with longitude, up to a constant grid distance of

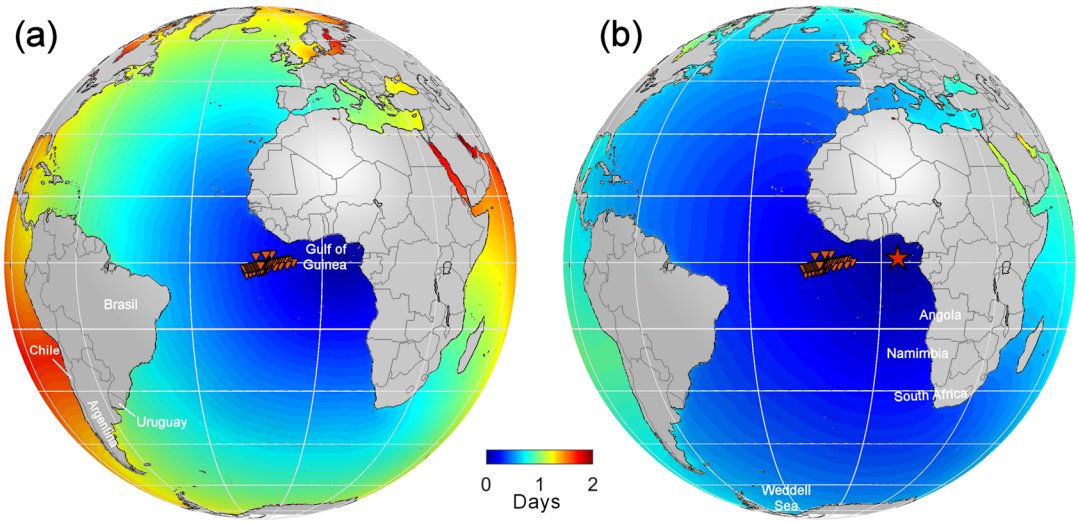

Figure 3. Calculated infragravity wave travel times in days, from a hypothetical source for period (a) $T = 100$ s, and (b) $T = 200$ s. inverted triangles show the location of the PI-LAB stations and the star marks the location of the hypothetical source, which is the same for both periods.

~25 km in the region that roughly covers all the Atlantic Ocean. The resolution of the back-projection method in this scale is significantly lower than the fine resolution of the bathymetry grid therefore a finer grid would not contribute to the precision of the results. Next, the depths are translated to group velocities for the central frequencies (f_p) of 5, 6.7, 8, and 10 mHz (or equivalently periods of 200, 150, 125, and 100 s). The travel times from each station to all grid-points, required from Equation 3, are calculated using Graph Theory and Dijkstra's algorithm. Figure 3 shows the estimated travel times from a hypothetical source, calculated for the shortest and longest periods examined in this work, that is, the shortest path method (Dijkstra, 1959; Moser, 1991).

3.3. Array Geometry Effects and Weighting

To evaluate the effects of the array geometry on the results of the incoherent beamforming and back-projection, the isotropic response of the array is calculated by assuming an isotropic distribution of plane waves. The corresponding theoretical correlation function C_n, for each station pair n, at lag time t can be calculated as (Harmon et al., 2012),

$$C_n^{theor}(t) = \frac{1}{\pi\sqrt{T_n^2 - t^2}}, \tag{6}$$

where T_n is the group arrival time of a direct wave arrival along the station pair, calculated as mentioned above.

The synthetic correlation functions are filtered with the same narrow bandpass filter that is applied to the true NCFs, around the same frequencies, and then the envelope of the signal is calculated by means of the Hilbert transform. Then, the isotropic response of the array is calculated by applying incoherent beamforming method as it was described earlier. Figures 4a and 4b show the isotropic response of the array for the period of 150 s, which is in the middle of the examined periods range, and it is indicative of all periods examined in this work. It reveals the expected bias because of the elongated geometry of the array, which amplifies the energy along specific azimuths. A more symmetric and evenly distributed array would be better optimized to accurately back-project infragravity waves and would have produced a uniform distribution of the energy across all azimuths, for a specific slowness.

Similarly, to investigate the array-geometry bias to the back-projection, the synthetic data are back-projected in the same way as the real data, using Equation 3, to generate the isotropic response as,

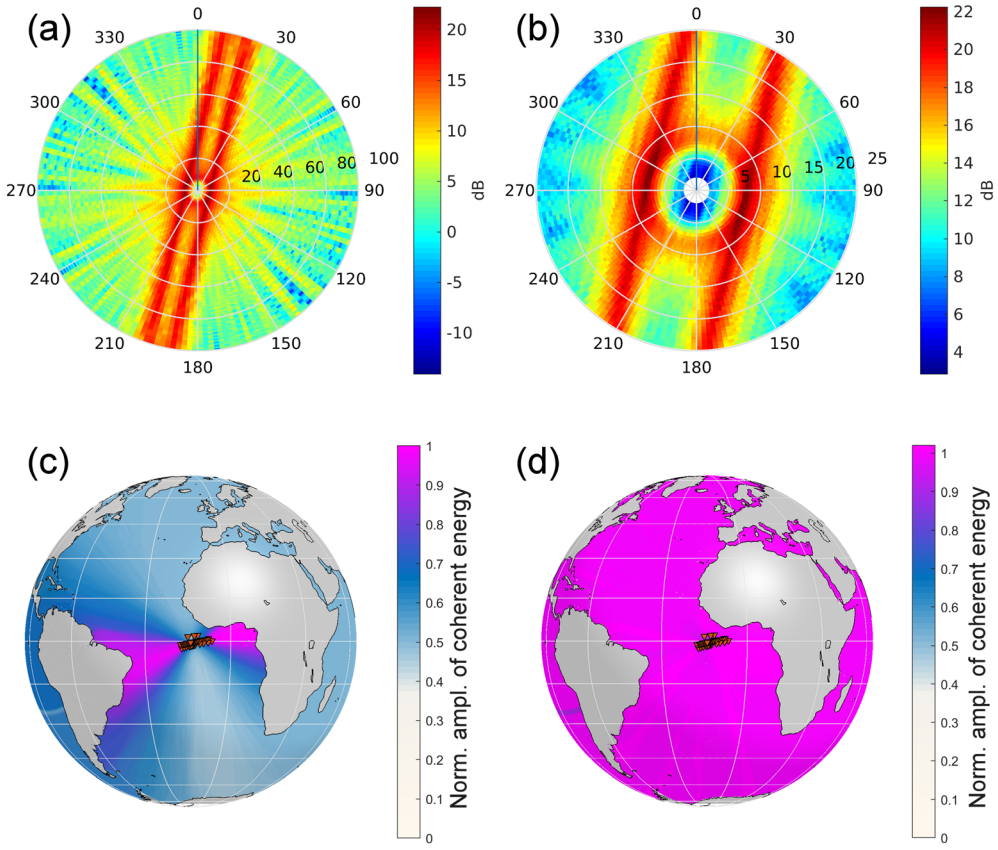

Figure 4. Beamforming response (top row) and back-projection response (bottom row) of the PI-LAB array for 150 s period. Beamforming response is shown (a) over a wide range of slowness and (b) zoomed in a limited range of slownesses where more details are visible. Back-projection response is shown (c) using non-weighted NCFs and (d) using the weights that were estimated by solving Equation 8.

$$P^{syn}(\varphi,\theta,\omega)=\sum_{n=\{i,j\}}\left\langle C_n^{theor}\left(t_i(\varphi,\theta,\omega)-t_j(\varphi,\theta,\omega)\right)\right\rangle. \tag{7}$$

In the ideal case, the shape of P^{syn} should correspond to the assumption made above of an isotropic distribution of sources. However, the elongated geometry of the array along the WSW-ENE direction causes artifacts such as a misleading amplification over this direction (Figure 4c). A similar effect also seen in the beamforming method. This problem can be mitigated by properly weighting each cross-correlation C_n^{theor}, before summation. The determination of the weights $\mathbf{W}=[Wn]^T$ corresponds to solving the following system of linear equations (e.g., Neale et al., 2015),

$$\begin{gathered}\mathbf{C}^{theor}\cdot\mathbf{W}=\mathbf{P}^{iso},\\ \text{subject to } W_n\geq 0 \text{ for all station pairs } n=\{i,j\}.\end{gathered} \tag{8}$$

The right-hand side of Equation 7 corresponds to the ideal back-projection result, that is, $\mathbf{P}^{iso}=[P_1,P_2,P_3,\ldots P_N]^T=[1\ 1\ 1\ldots 1]^T$. Because of the requirement for nonnegative weights, Equation 7 cannot be solved by means of linear programming. In this work, we introduce a two-stage technique that uses an initial estimate of the weights and then, further optimizes them using the Trust Region Reflective (TRR) Algorithm (Coleman & Li, 1994, 1996) which solves the problem by means of quadratic programming, as it is implemented in MATLAB 9.2 [https://uk.mathworks.com/help/optim/ug/least-squares-model-fitting-algorithms.html#broz0i4, last accessed on January 2019]. This approach requires an initial estimate for $\mathbf{W}$, which is obtained by solving Equation 7 in a linear way, omitting the nonnegative constraint and using the Moore-Penrose pseudo-inverse (Moore, 1920; Penrose, 1955) to invert $\mathbf{C}^{theor}$. It is possible that $\mathbf{W}$ from

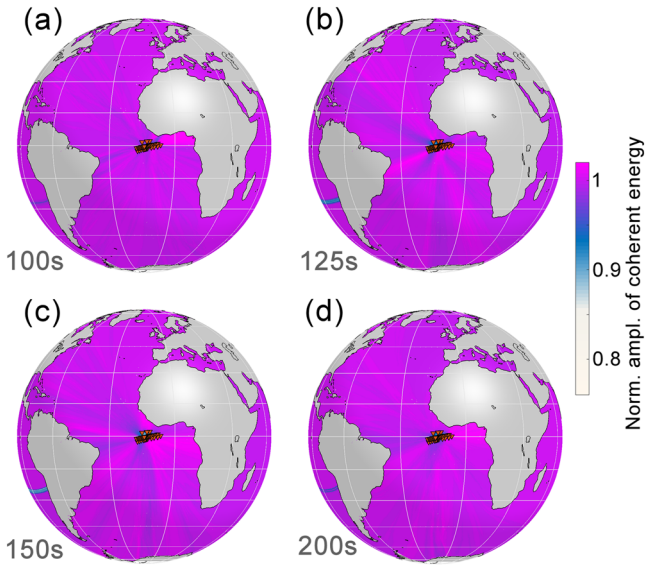

Figure 5. Back-projection results of isotropic source synthetic data with the optimal weights, for central periods of (a) 100, (b) 125, (c) 150, and (d) 200 s.

the linear inversion happens to satisfy the non-negative condition. In this case, the nonlinear optimization step is not needed. Otherwise, the TRR algorithm is applied. The latter allows the setting of a priori lower and upper bounds for the weights. We set these bounds by trying to enclose most of the range of values of the linear solution to satisfy the nonnegativity constraint and to ensure that we use all available pairs of stations, that is, the minimum weight should not be null. After estimating the optimal **W**, we recalculate the back-projection for the isotropic case. The result is now significantly improved (Figure 4d). The same weights are then used in Equation 3 to back-project the real data, yielding a normalized amplitude of coherent energy (thereafter, also referred to as just "energy" for convenience; the term "energy" refers to the normalized amplitude of coherent energy in the case of the back-projection method or just the coherent energy when it refers to the beamforming method), minimizing the artifacts due to the array geometry. This procedure of properly adopting the weight of the contribution of each pair of stations is applied for each central frequency. The back-projection results for the isotropic case, after optimizing the weights, for each of the periods that are examined in this work are shown in Figure 5. In all examined periods, the result accurately images the isotropic source input, with only minor indistinguishable variations.

Furthermore, to investigate the smearing direction and the resolution of the back-projection, we calculate synthetic cross-correlograms from hypothetical sources of Gaussian shape and peak amplitude = 1, located at various places with respect to the PI-LAB array. The source wavelet is propagated from the source to the array, and then the energy is back projected onto the grid. The results are shown in Figure 6 and suggest that for sources located along the East-Northeast and West-Southwest direction, with respect to the PI-LAB array, there is significant smearing along the same direction, as it is expected from the geometry of the array (Figure 6b). In contrast, sources that are located orthogonally to this direction are imaged more accurately without suffering from significant smearing. This also results in a higher peak amplitude as the energy is concentrated over a notably smaller region (Figure 6a).

4. Results

The beamforming shows significant coherent energy, which arrives from all directions and over a wide slowness range (Figures 7 and 8). The spectrogram of the beam power shows a large number of high-energy arrivals distributed generally in an arbitrary way during the period of the PI-LAB experiment without any significant seasonal or any other pattern (Figure 7, top). These peaks in power are spread along a range of periods and are roughly >11 db for periods shorter than ~150 s and >9 db for periods around 200 s. There is a relatively high-energy region at the first month of the deployment which is attributed to the releveling procedure and higher noise for some stations. Back azimuths present a bimodal distribution with the energy arriving from ~70° during most of the year at periods 100 s and greater. However, there are distinct times, which we refer to as "events" during which energy arrives from ~250°. We observe less of a pattern at shorter periods (Figure 7, middle).

The beamforming analysis of the back azimuths reveals temporal changes in the azimuth of the coherent energy in the form of distinct events, well-defined in time, with limited duration (of the order some days up to a couple of weeks) with back azimuths around 250°. These events appear more frequently from October to February, and they are characterized from similar beam power as other events with other back azimuths. There are at least three such, relatively long events, with durations of several days each. The dominant apparent velocity is between 100 and 140 m/s (Figure 7, bottom) and does not show any notable variation during their occurrence.

Polar plots of the 361-day stack of the beamforming output show the power of the beam as a function of azimuth and slowness (Figure 8). An elongated structure along the direction 70°–250° is the most prominent feature, which is present in all examined periods. The largest amount of energy appears to arrive from the

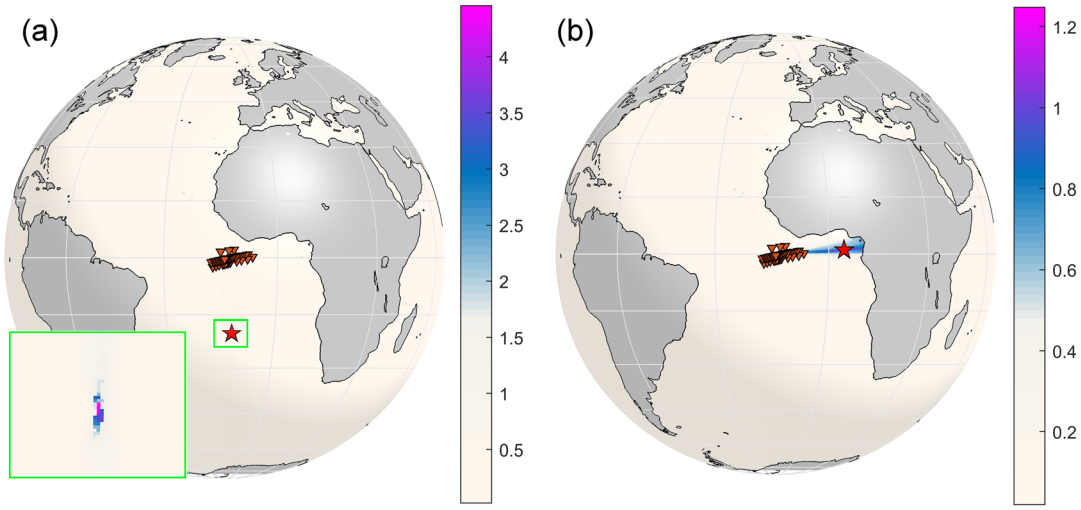

Figure 6. Back-projection results for synthetic timeseries data corresponding to hypothetical Gaussian shaped sources (red star) located (a) south of the array and (b) at the Gulf of Guinea (right) using the back-projection method. The inset image in (a) shows the zoomed version of the green rectangle that encloses the source on the map. Color corresponds to the amplitude of the stack.

East, across a wide range of azimuths, with a peak at the azimuth of ~70°, as noted earlier. The apparent slowness of the peak energy decreases with increasing period, from ~13 s/km at 100 s to ~7 s/km at 200 s period, which is expected from the dispersion of infragravity waves. It should be noted that the geometry of this feature is close to the bias direction of the array for the expected slowness range of infragravity waves (Figures 4a and 4b); therefore, it is difficult to conclude solely by the beam-forming results which portion of this energy is real and which is an artifact due to the selective amplification and smearing along these azimuths. However, through the use of the back-projection technique and by properly

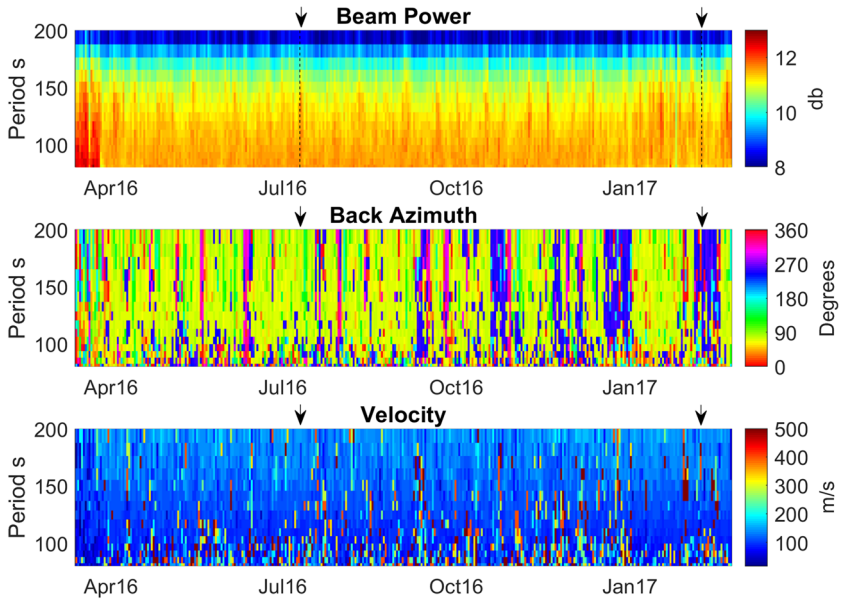

Figure 7. Summary of beamforming results. (Top) Plot of beam-power (db) as a function of time and period. (Middle) plot of back azimuth direction as a function of time and period. (Bottom) plot of apparent velocity (m/s) as a function of time and period. Arrows show 2 days (on 10 July 2016 and 8 February 2017) that correspond to the two dominant back azimuths and are examined separately later.

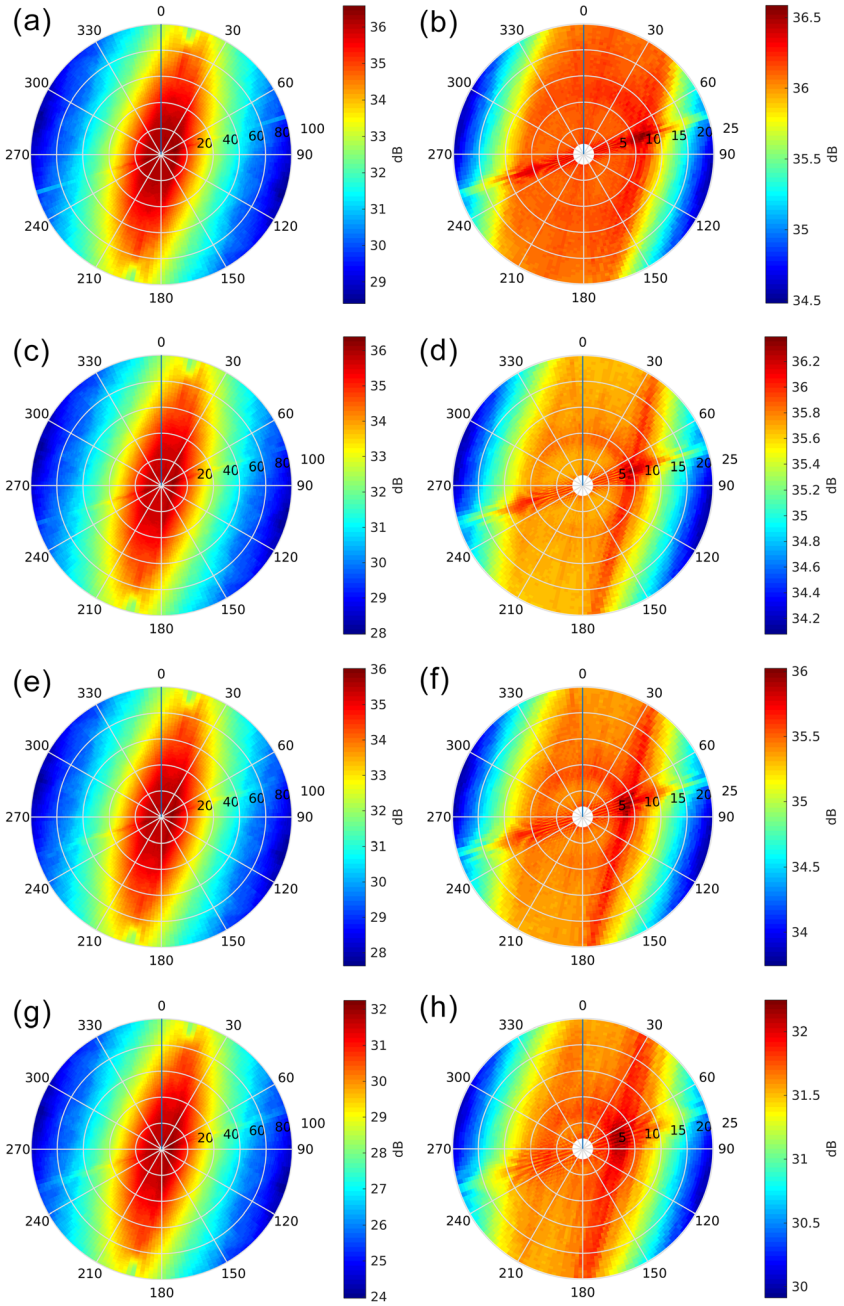

Figure 8. Azimuth (degrees) vs slowness (s/km) polar plots of 361-day stack of the beamformer output (db) of the PI-LAB array, for 100 s (a, b), 125 s (c, d), 150 s (e, f) and 200 s (g, h). The left column shows a wide slowness range, while the right column repeats the plot on the left but zoomed in the center, where more details can be seen.

adopting the weights of the station pairs, as described earlier, we are able to mitigate the effects of the array geometry.

We initially examine the dominant sources for the entire period of the deployment. Therefore, we back-project NCF stacks throughout the maximum span of the experiment. Back-projection results after the correction for the isotropic case (Figure 9) show an asymmetric distribution of infragravity wave sources, with the most dominant directions pointing at the Southern Hemisphere. On the contrary, significantly less coherent energy arrives from the Northern Hemisphere. We interpret the energy which exceeds the ~50% of

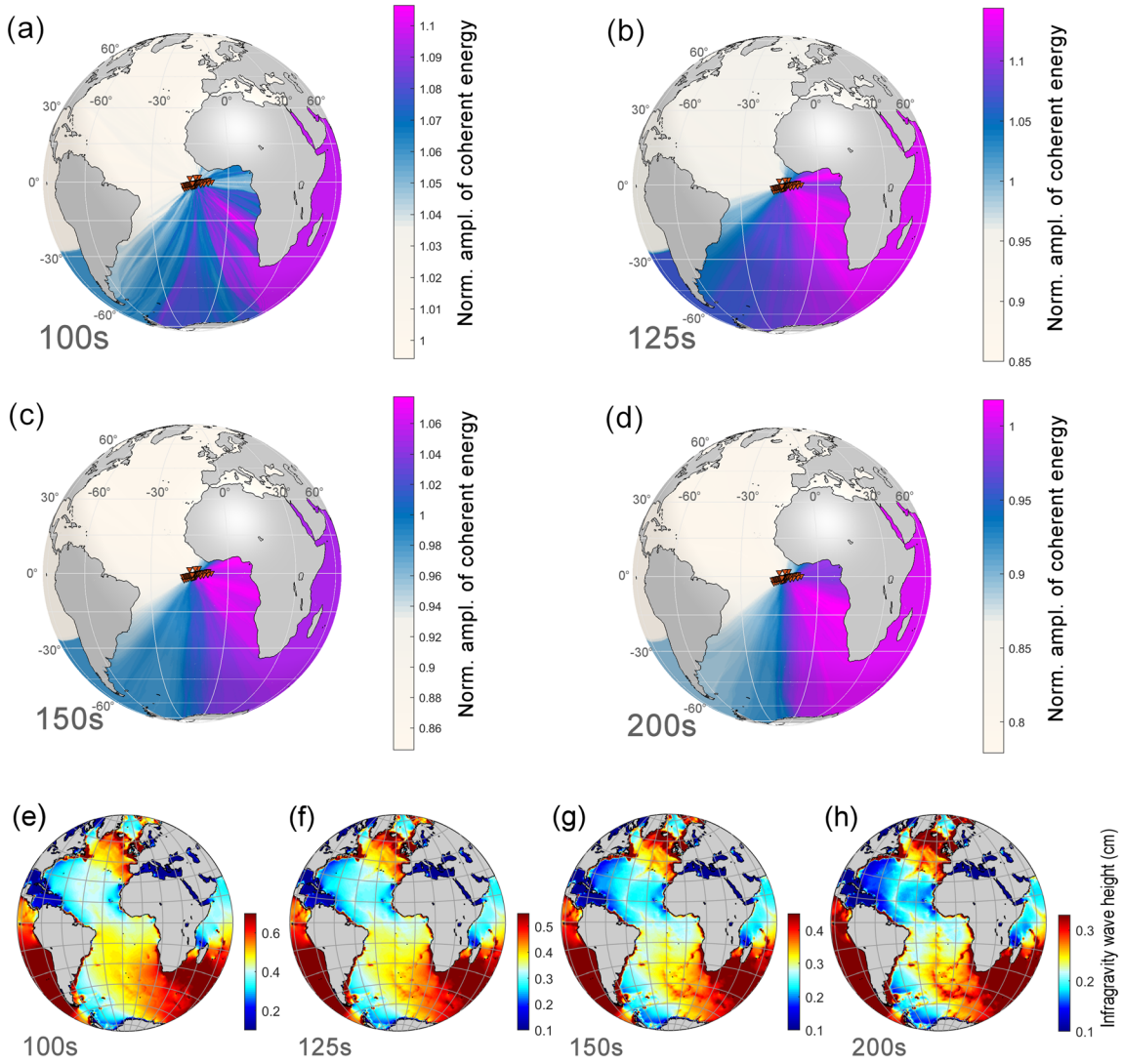

Figure 9. Back-projection results for the periods of (a) 100, (b) 125, (c) 150, and (d) 200 s. (e–h) WAVEWATCH III Infragravity wave height model averaged over the duration of the PI-LAB experiment (i.e., March 2016–March 2017; Ardhuin et al., 2014; downloaded from http://ftp://ftp.ifremer.fr/ifremer/ww3/HINDCAST/GLOBAL_IG, last accessed on October, 2019).

the range of the normalized amplitude of coherent energy. Specifically, the dominant sources are in the west coast of Africa and, in a lesser extent, in Antarctica and the east coast of South America, at latitudes, lower than −5°. At 100 s period, the more coherent sources are located off the coast of Namibia, the coast of South Africa as well as in Antarctica and from the Weddell Sea coast. There is also considerable energy that arrives from sources in the Indian Ocean at the south coast of South Africa. There is also some energy from sources at the coasts of Argentina and to a lesser extent from Uruguay and Brazil. At 125 s period, the main sources are in the Gulf of Guinea, and then from the coast of Angola down to the coast of South Africa. There are also more consistent arrivals from the southern coast of South America with sources located at latitudes lower than −5°. Again, considerable amount of coherent energy arrives from sources at the coast of Antarctica. At 150 s period, the sources show a relatively similar pattern to the previous case, with less incoming energy from south of South Africa. At 200 *s*, the predominant energy arrives from sources along the coast of Angola, Namibia and South Africa, as well as the Antarctica coast at longitudes between 0 and 60°E. Again, a significant amount of coherent energy arrives from south of the South African coast, possibly from sources in the Indian Ocean. There are also coherent energy arrivals from a small section of the east coast of South America, at latitudes lower than −20°.

We compare our year-long average back-projections to the corresponding 1 year-long average WAVEWATCH III Infragravity wave height model (Figures 9e–9h; Ardhuin et al., 2014; downloaded from http://ftp://ftp.ifremer.fr/ifremer/ww3/HINDCAST/GLOBAL_IG, last accessed on October, 2019). We calculate the average infragravity wave height by integrating the surface elevation spectrum over the desired frequencies and time (e.g., equation (1) in Ardhuin et al., 2014). The key features in the model are increased heights in the open ocean mostly at the Southern Hemisphere, and significant possible sources at the coasts of Namibia and South Africa, as well as the coasts at the Gulf of Guinea. There are also source regions along the Atlantic coasts of South America. In the Northern Atlantic, the regions of relatively large wave heights are limited to a region between Europe, Greenland, Canada, and Morocco and extend to a lesser degree southwards.

Finally, there are significant wave heights in the Pacific and the Indian Ocean. The Indian Ocean appears to leak more infragravity wave energy into the Atlantic than the Pacific. This pattern does not vary significantly for the maps from 100–200 s periods. This contribution to the infragravity wave energy from other ocean basins is supported by the model of Ardhuin et al. (2014) which shows wave heights that gradually scale from >0.6 cm at 100 s to >0.3 cm at 200 s at both the southeastern coast of Africa and the Indian Ocean, as well as the coast of Chile and the Pacific Ocean (Figures 9e–9h). It should be noted that the resolution of our method deteriorates with increasing distance from the array. Thus at large distances the result tends to be smoothed out. This is because the ray paths of two sources with relatively small spatial separation to each other, located at large distances from the array, will share nearly identical trajectories close to the array. Therefore, they will produce nearly identical noise cross-correlation functions, and consequently the back projection will show then as one large region instead of two separate peaks.

The features in the infragravity wave models are generally consistent with source regions determined with back-projection. For instance, in the Southern Hemisphere, our back-projection detects sources from South America south of ~15°S latitude but does not detect sources near the equator. There is also a large region of relatively high infragravity waves in the model (e.g., height > 0.55 cm for the period of 100 s) in the open ocean south of the PI-LAB array, which appears to be related to sources and/or reflections from both the Atlantic coasts of Africa and to lesser extent South America. Our back-projections at 125–200 s period also detect most of the significant wave heights radiating from the coasts of Africa and the region that extends south, down to the Antarctic coast at longitudes larger than 0° in the infragravity wave model at the same periods. In our back projections, coherent energy arrives from the Weddell sea particularly for the periods of 100 and 125 s, and to a lesser extent for 150 and 200 s, but corresponds to relatively low <~0.2 cm infragravity wave height this region in the infragravity wave model regardless the examined period. Our back-projection results have lack of coherent energy from the Northern Hemisphere across all tested periods in the back-projection results, which may be a result of the limited spatial source region visible in the infragravity wave model.

As we mentioned earlier, beamforming analysis reveals a temporal variation with a handful of distinct events from October to February from a back azimuth around 250° that disrupt the typical east and southeast back azimuths during the rest of the year. To further investigate this pattern, we explore the back-projection of daily stacks to probe variations in source locations through time. We back-projected the infragravity energy for two example event days, one in February and one in July (Figures 10c and 10d). The first on the 10 July 2016 and the second on the 8 February 2017 present significantly different results (Figure 10). We compare our results to the modeled infragravity wave height (Ardhuin et al., 2014; downloaded from ftp://ftp.ifremer.fr/ifremer/ww3/HINDCAST/GLOBAL_IG, last accessed on October 2019), on the same and the previous day, all sampled at 18:00 UTC.

On 10 July 2016, most of the coherent energy appears to arrive from the Southern Hemisphere, with predominant sources at the Gulf of Guinea, Namibia and South Africa (Figure 10c). This agrees with significant infragravity wave heights in these regions along the western coast of Africa (i.e., >0.8 cm; Figure 10a). Whereas, moderate IG amplitudes (>0.55 cm) across the Atlantic Basin in July (Figure 10a) in comparison to lower amplitudes in February (<0.50 cm; Figure 10b) are suggestive of leakage of IG wave energy off the western coast of Africa across the Atlantic Basin to the PI-LAB array. There are also significant arrivals from the Atlantic coast of South America, which again agrees with sources modeled along these regions. Significant infragravity wave heights that are modeled south and east of South Africa, and the Indian

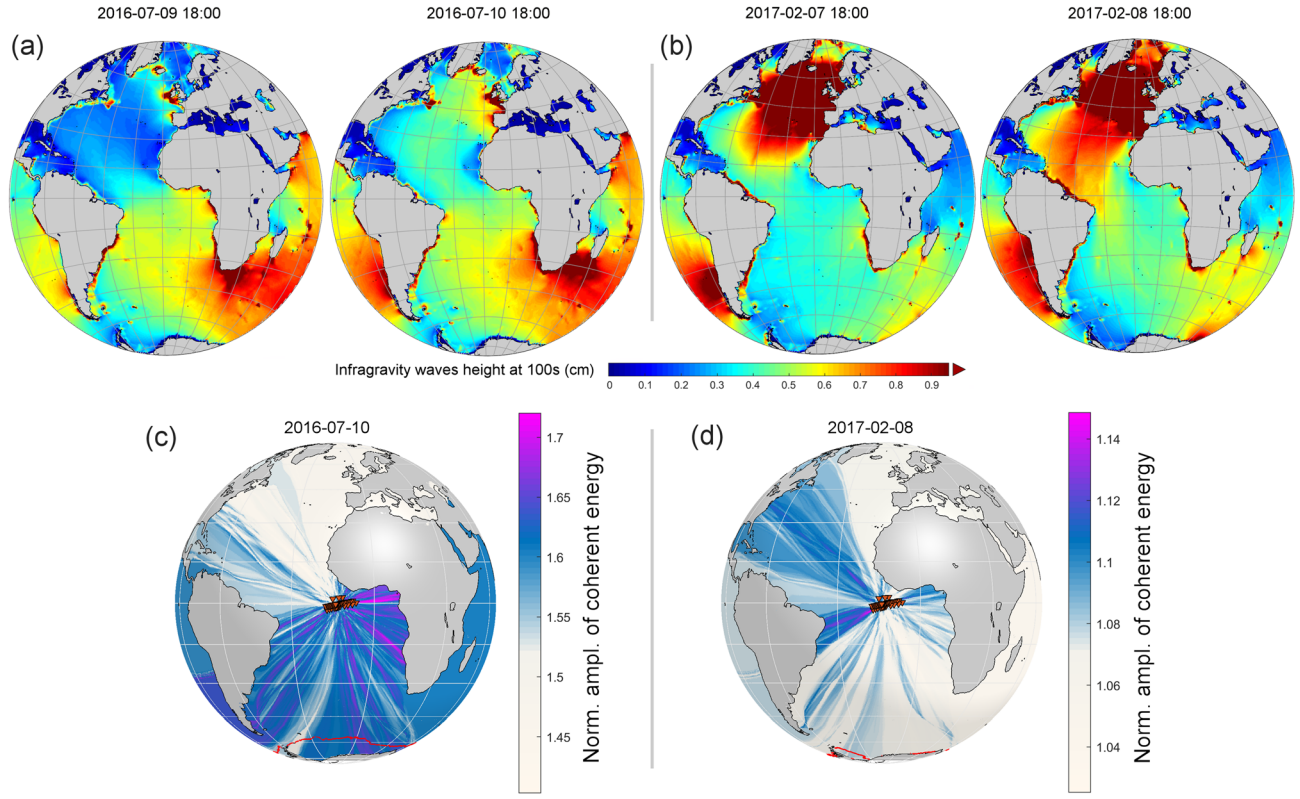

Figure 10. (Top row) WAVEWATCH III Infragravity wave height model for ~100 s period (Ardhuin et al., 2014; estimated as discussed in the main text, from the wave elevation spectrum that was downloaded from http://ftp://ftp.ifremer.fr/ifremer/ww3/HINDCAST/GLOBAL_IG, last accessed on October, 2019), (a) On 9 and 10 July 2016 and (b) on 7 and 8 February 2017, all at 18:00 UTC. (Bottom row) Back-projection results for the period of 100 s, during (c) the 10 July 2016 and (d) the 8 February 2017. The red line shows the effective ice boundary, calculated by averaging the open ice cover with the close and fast ice, using data from Aaboe et al. (2018).

Ocean, as well as the Southern Pacific Ocean, appear to correlate with relatively high coherent energy that is mapped in these areas from the back-projection. It should be noted however that as mentioned earlier, at large distances compared to the aperture of the array, the resolution of the back-projection method deteriorates, and thus it is expected energy from point sources to be smeared over larger regions. Coherent energy that is mapped at the Antarctic coast does not correspond to modeled open ocean infragravity wave heights, especially in negative longitudes. A source region near the coast of Canada appears slightly in the back-projection results, but similar sources in Europe and Greenland are not shown, possibly due to the shadow zone that the African continent creates for these azimuths for the PI-LAB array.

On 8 February 2017, the situation is reversed. Predominant sources in the back-projection are located at the most eastern coast of Brazil, and the North Atlantic Ocean, whereas very little energy arrives from the south. This appears to largely agree with generally higher infragravity wave height (>0.6 cm) in Northern Hemisphere and significantly smaller wave heights (mostly in the range 0.2–0.55 cm) in Southern Hemisphere during the period of the back-projection (Figure 10b). The region with the largest coherent energy in the back-projection is the coast of Brazil, which appears to be related with the infragravity wave energy that arrives from a weather system in the North Atlantic ocean at the northern coast of South America, and then reflects/refracts toward the Equatorial and South Atlantic ocean (Figure 10b). There are large infragravity wave heights >0.7 cm on the coasts at lower latitudes as well, which do not correlate with high amplitudes in back-projection results, indicating limited infragravity wave leakage to the open ocean from these regions. This is also evident from the low infragravity wave heights (~0.3 cm) further away from these coasts (Figure 10b). Coherent energy in our back-projections from the Northern Hemisphere appears to be correlated with significant infragravity heights >0.65 cm, near and off the coasts of the United States of America, Canada. The main contribution appears to be from infragravity waves that are

generated from a weather system between Europe, Greenland, and Canada, which gradually propagate southwest, eventually reaching the northern coasts of South America as mentioned earlier. As with the contrary previous case, our back-projection results do not show sources in European coasts and Greenland, despite the modeled infragravity wave heights in these regions, which as mentioned earlier could be due to the shadow zone that the African continent creates for this range of azimuths to the PI-LAB array.

5. Discussion

Using data collected by the PI-LAB experiment at the equatorial mid-Atlantic Ridge, we observe infragravity wave energy arriving from sources around the Atlantic, but with the most coherent sources in the Southern Hemisphere. Depending on the examined period, the sources are located in the west coast of Africa, Antarctica, and the southern part of the east coast of South America. Prominent sources are found in the Gulf of Guinea, the coast of Namibia and the Coast of South Africa. Comparison to the infragravity wave height model from WAVEWATCH III (Ardhuin et al., 2014) reveals generally good agreement between source regions indicated by the back-projection and large wave heights in the infragravity model in both the year-long averages and also in daily stacks. In particular, our array is able to identify strong source regions of leaking infragravity waves near the Atlantic coasts of Africa visible in the infragravity wave model. This is probably not due to the closer proximity of PI-LAB array to the African coast, given that the waves experience little attenuation (e.g., Godin et al., 2013). Instead, it is probably due to high degrees of leakage due to the continental slope bathymetry, and the concaveness of the west coast of Africa, as opposed to the convex geometry of the east coast of South America (Ardhuin et al., 2014). This region has been also identified as a significant potential source of leaked deep ocean infragravity waves in other studies (e.g., Crawford et al., 2015). We are also able to identify strong ephemeral sources in regions that do not exist in the year-long stacks, such as the sources in North America at the 8 February (Figures 10b and 10d).

To quantify the correlation between the back-projection result and the infragravity wave height model, we plot the year-long averages of the infragravity wave model versus our back-projection energy for periods of 100, 125, 150, and 200 s, and for a region of up to 30° from the center of the array (Figure S2 in the supporting information). A linear trend is visible in the plot, although with significant scatter, regardless the period. We remove outliers using a conservative approach of excluding anything beyond three times the typical range of 1.5× (~or ~2.7σ in a Gaussian distribution) above the upper quartile or below the lower quartile. This corresponds to the 0.8%, 1.3%, 1.9%, and 2.3% of the total data points for each period, respectively. Next, we calculate the correlation coefficient, which ranges between 0.56 and 0.59 for the different examined periods. The correlation coefficients suggest that even though we have used only phase information, the back-projection of the amplitude normalized pressure data yields some information about the wave heights of the infragravity wavefield. In other words, large wave heights produce more coherent energy and therefore larger back-projection amplitudes. The correlation coefficient is likely reduced by the amplification of weaker wave fields by the amplitude normalization during the preprocessing stage of our data.

There are notable differences between the back-projection source regions and the infragravity wave model. Particularly, in the single day stacks, our back-projection identifies a coherent source region coming from the coast of the United States of America on 8 February 2017, where no large wave heights are visible in the infragravity wave model. In addition, we do not observe the effects of the large source between Greenland and Northern Europe on this day in our back-projections. Our observations can likely be explained by reflections off the coast of the United States of America from the strong sources visible in the infragravity wave model between Greenland and Northern Europe. The African continent likely prevents the PI-LAB array from imaging sources in European coasts and Greenland, as it creates a shadow zone along these azimuths.

Another interesting difference between our back-projections and the infragravity wave model is that there is a considerable amount of coherent energy that arrives from the shoreline of Antarctica and Weddell Sea. To the knowledge of the authors, there is no known mechanism that can excite infragravity waves from the ice-selves, something that is also confirmed from the infragravity wave models (Ardhuin et al., 2014). Therefore, this energy could correspond to infragravity waves that are generated elsewhere, travel transoceanic distances to be reflected back from Antarctica. Depending on the period of the year, the sea ice surrounding the coast of Antarctica can extend to more than 1,000 km from the coast during the Northern Hemisphere

summer and retreat but not completely disappear during the Northern Hemisphere winter (e.g., Aaboe et al., 2018). Note that in Figure 10a, there is a significant amount of energy coming from Antarctica even close to the sea ice maximum. It has been shown that the reflection coefficients of infragravity waves when they meet sea ice decrease with period and for periods larger that ~30 s are expected to be effectively null for a wide range of ice thicknesses, yielding 100% transmission (Fox & Squire, 1990, 1994). This suggests that the energy recorded at the PI-LAB array might correspond to infragravity waves that propagate through sea ice for up to thousands of km (e.g., Aaboe et al., 2018) with little attenuation and reflect from the Antarctic coast. Such unattenuated propagation of infragravity waves through the sea ice has also been suggested by Wadhams and Doble (2009), who utilize tilt observations from instruments located on the sea ice, near North Pole to infer the infragravity wave propagation in that region. Numerical modeling similarly supports the notion of infragravity wave travel though sea ice (Squire, 2007; Squire et al., 2009) These studies showed that short period (e.g., <15 s) surface waves attenuate due to scattering by the broken floes and ice thickness variations or are damped by ice inelasticity, turbulence, and friction within a few tens of km of the marginal ice zone; whereas, infragravity energy of longer periods (20–30 s) can propagate for more than ~1,600 km of sea ice cover without any significant attenuation (Squire, 2007; Squire et al., 2009). In the present work, the infragravity energy that is examined is of even longer periods (100–200 s). Thus, it is expected to exhibit similar behavior. The two-way path propagation of infragravity waves within the Antarctic sea ice could play a significant role in the integrity and the dynamics of the sea ice and requires further investigation. Future work using OBS to measure the two-way travel time of reflected waves from the sea ice ocean bottom pressure gauges may provide a novel, passive, and remote means to measure sea ice thickness in situ (e.g, Wadhams & Doble, 2009).

The variations of the back-projection results from the modeled infragravity wave height can be attributed to various factors. Although we have minimized bias with our new optimized back-projection methodology that weights station pairs to account for the linear geometry of the array, it is not possible to completely remove it, and as we mention previously, it is likely that some bias remains. Furthermore, limitations in resolution and the noise in data can also produce differences. Physically, regions with high coherent amplitudes from the back-projection but low infragravity heights could be indicative of coasts that act as reflectors rather than sources of infragravity waves. An example of that is probably the coast of Antarctica as mentioned earlier. Other factors that can cause differences could be related to empirical choices for reflection coefficients in the model, variations in the effectiveness of the propagation path, the fact that the model does not take into account accurately the coastal morphology or the direction/spread of the forcing short-period waves, which have been found to be important for the generation of deep ocean infragravity waves (e.g., Ardhuin et al., 2014; Crawford et al., 2015). Crawford et al. (2015), argues that in several cases, the coastal morphology and orientation dominate in the radiation of deep ocean infragravity waves, over factors such as the height of the source waves or the effectiveness of the propagation path. In the future, incorporating amplitude information into our method would likely enhance the correlation with the infragravity wave model (Ardhuin et al., 2014).

Coastal reflections, if they can be accurately measured, could provide a constraint on the reflection coefficients used in infragravity wave modeling. We test the occurrence of reflected infragravity waves from the coast of Africa, by assuming a simple reflection geometry, where a transient wave passes through the PI-LAB array, reaches the coast and reflects, and travels back to the array along the same ray path. In this case, for a given pair of stations that are located along the ray path, the reflected phase is expected to be observed at lag time t_1+2t_2, where t_1 is the travel time of the wave between the stations and t_2 the travel time from the shoreward station to the shore (e.g., Neale et al., 2015). To identify possible reflections, we calculate a year-long stack of NCFs of approximately 14 hr, band-pass filtered with central period of 200 s, where the noise is less compared with shorter periods. We then correct for the relative azimuth between the station and the reflected IG waves, under the plane wave approximation, in order for the reflected phases to be aligned across the expected moveout line (approximately the same as the direct phases). We apply this procedure for seven test azimuths that represent potential reflection points in African and South American coasts (Figure 11). From the visual inspection of the NCF's, we could not clearly identify any such reflections (Figure S1). However, to further investigate for reflected energy that may be hidden under the noise, we apply a linear Radon transform to the NCF's (e.g., Gu & Sacchi, 2009), that is, we stack the traces along different velocities (moveouts) within the range of the expected average velocity values and produce the

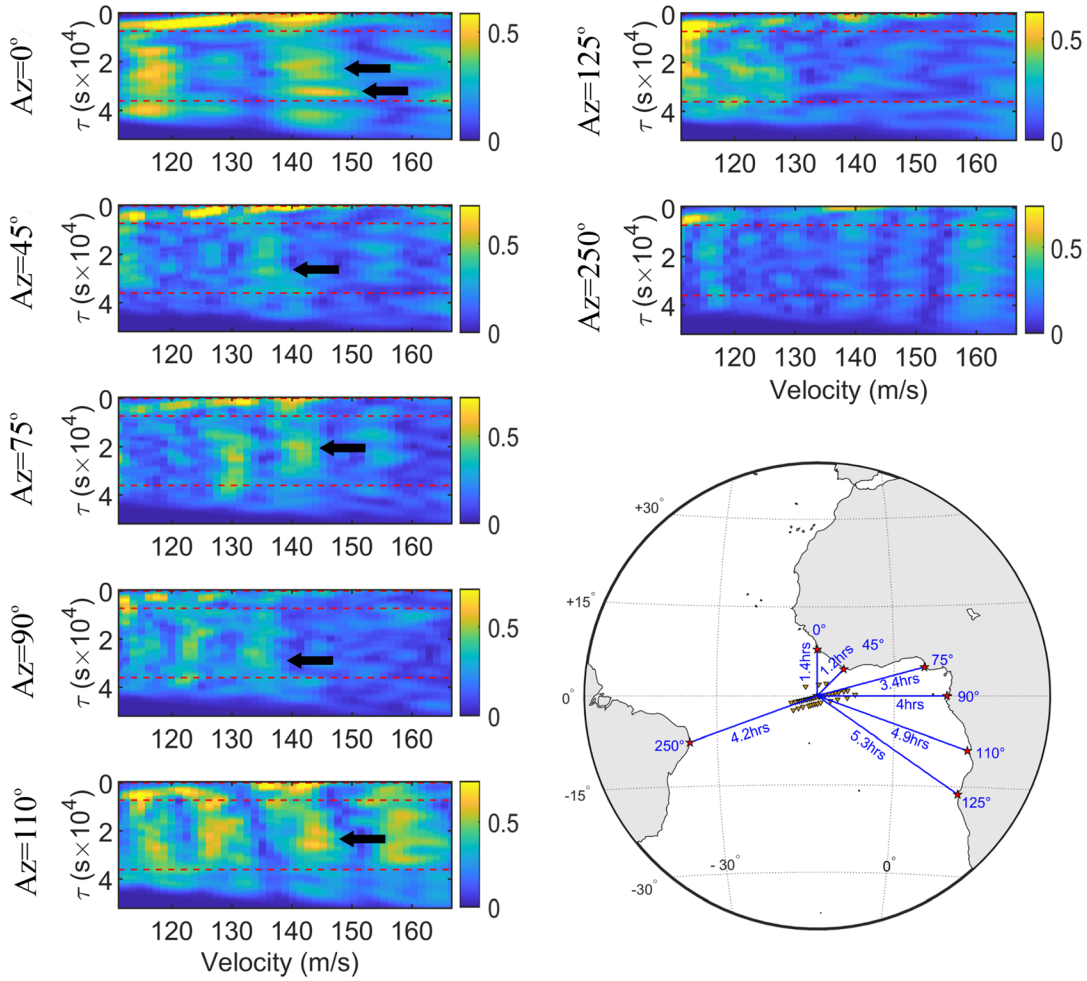

Figure 11. Linear Radon transform of ~14-hr long NCF's, after projecting the interstation distance to the great arc of a reflected plane wave arriving from azimuth shown at the beginning of each panel. The vertical axis corresponds to the radial coordinate projected to the time vector, considering a velocity of ~140 m/s. Color corresponds to the stacked absolute amplitude of the NCF's. The two dotted lines correspond hypothetical reflections, calculated for one-way travel time of 1 and 5 hr, respectively. Arrows show some peaks at the expected velocity and time of reflected phases. The inlet map shows the tested reflection points (stars), with their azimuths and their travel times from the center of the PI-LAB array (inverted triangles).

amplitude of the stack as a function of the velocity and time (Figure 11). Significant peaks can be identified at near zero time in almost all tested azimuths corresponding to the moveout of the direct phase. The corresponding moveout velocity is near the expected values ~140 m/s (e.g., Figure 7 bottom). By aligning the signals to the reflected phase direction (changing the beam of the array), the alignment of the direct phase is deteriorated, and thus, it is not accurately mapped into the Radon domain. We identify clear peaks that correspond to velocities and times that are to be expected in the presence of reflections from the African coast at the azimuths of 0°, 45°, 75°, and 110° (Figure 11). Variations in velocity can be attributed to various factors. For example, if the real propagation direction is different from the assumed, it will have a faster apparent velocity. Other factors can be the stronger dispersion of the reflected waves due to the longer paths they travel, as well as multiple reflections from different azimuths, and/or curved wave fronts. On the contrary, there are no such peaks at the azimuth of 250° that points on the coast of Brazil. Similar analysis for reflections at the Antarctic coast was not possible due to its large distance from the array, the unfavorable orientation of the stations, and the fact that both incident and reflected waves for many of the sources will arrive from the same direction. These results suggest that reflected infragravity waves contribute to the energy recorded in the deep ocean. This also suggests that future work examining

reflection amplitudes from well-calibrated ocean bottom pressure records will better constrain reflection coefficients.

6. Conclusions

We observe open ocean infragravity waves at the equatorial mid-Atlantic using ocean bottom pressure records and present a new global back-projection method, based on graph theory, for determining source locations for infragravity waves. Our method uses a two-stage, adaptive weighting scheme to minimize the effects of the array geometry.

The dominant source region over the yearlong deployment is the western coast of Africa, with some coherent energy from South America. We also find evidence for transient infragravity waves generated or reflected from North America and indications of waves that may have traveled through sea ice, reflecting off Antarctica. Our results generally agree with previous works (e.g., Ardhuin et al., 2014; Crawford et al., 2015). The continental coastal morphology is the most likely reason for the difference in leaked infragravity wave energy. The concave morphology of the Gulf of Guinea in Africa likely focuses and reflects infragravity wave energy and potentially leaks more refracted wave energy due to sharp changes in coastline orientation versus the convex morphology of Brazil in South America. We find evidence for such reflections along various azimuths from the coast of Africa. Further study of the amplitude of such reflections could provide better constrains of coastal reflection coefficients that are used as empirical inputs in infragravity waves models.

Data Availability Statement

The waveform data used in this study are available through the facilities of IRIS Data Services, and specifically the IRIS Data Management Center at https://doi.org/10.7914/SN/XS_2016. IRIS Data Services are funded through the Seismological Facilities for the Advancement of Geoscience and EarthScope (SAGE) Proposal of the National Science Foundation under Cooperative Agreement EAR-1261681. For the visualization of WAVEWATCH III infragravity wave data, the panoply software was used that was developed at the NASA Goddard Institute for Space Studies, downloaded from https://www.giss.nasa.gov/tools/panoply/ (last accessed on June 2019).

Acknowledgments

The authors would like to gratefully acknowledge the editor, Dr Kristopher B. Karnauskas, and three anonymous reviewers for their critical reviews that helped to improve this manuscript. The authors would also like to acknowledge funding from the Natural Environment Research Council (NE/M003507/1 and NE/K010654/1) and the European Research Council (GA 638665). The WAVEWATCH III infragravity wave height models, used in this study, are from the work of Ardhuin et al. (2014) and downloaded from http://ftp://ftp.ifremer.fr/ifremer/ww3/HINDCAST/GLOBAL_IG, last accessed on October, 2019.

References

Aaboe, S., Breivik, L.-A., Sørensen, A., Eastwood, S., & Lavergne, T. (2018). Global sea ice edge and type product user's manual, OSI-402-c & OSI-403-c, the EUMETSAT Ocean and sea ice SAF, online available at http://osisaf.met.no/docs/osisaf_cdop3_ss2_pum_sea-ice-edge-type_v2p3.pdf, last accessed on June, 2019.

Amante, C. & Eakins, B. W. (2009). ETOPO1 1 arc-minute global relief model: Procedures, data sources and analysis. NOAA technical memorandum NESDIS NGDC-24, National Geophysical Data Center, NOAA. https://doi.org/10.7289/V5C8276M, last accessed January, 2017.

Ardhuin, F., Gualtieri, L., & Stutzmann, E. (2015). How ocean waves rock the Earth: Two mechanisms explain microseisms with periods 3 to 300 s. *Geophysical Research Letters*, *42*, 765–772. https://doi.org/10.1002/2014GL062782

Ardhuin, F., Rawat, A., & Aucan, J. (2014). A numerical model for free infragravity waves: Definition and validation at regional and global scales. *Ocean Modelling*, *77*, 20–32. https://doi.org/10.1016/j.ocemod.2014.02.006

Aucan, J., & Ardhuin, F. (2013). Infragravity waves in the deep ocean: An upward revision. *Geophysical Research Letters*, *40*, 3435–3439. https://doi.org/10.1002/grl.50321

Biesel, F. (1952). Equations generales au second ordre de la houle irreguliere. *Houille Blanche*, *5*, 372–376.

Bromirski, P. D., Chen, Z., Stephen, R. A., Gerstoft, P., Arcas, D., Diez, A., et al. (2017). Tsunami and infragravity waves impacting Antarctic ice shelves. *Journal of Geophysical Research: Oceans*, *122*, 5786–5801. https://doi.org/10.1002/2017JC012913

Bromirski, P. D., Diez, A., Gerstoft, P., Stephen, R. A., Bolmer, T., Wiens, D. A., et al. (2015). Ross ice shelf vibrations. *Geophysical Research Letters*, *42*, 7589–7597. https://doi.org/10.1002/2015GL065284

Bromirski, P. D., Sergienko, O. V., & MacAyeal, D. R. (2010). Transoceanic infragravity waves impacting Antarctic ice shelves. *Geophysical Research Letters*, *37*, L02502. https://doi.org/10.1029/2009GL041488

Coleman, T. F., & Li, Y. (1994). On the convergence of reflective Newton methods for large-scale nonlinear minimization subject to bounds. *Mathematical Programming*, *67*(1-3), 189–224. https://doi.org/10.1007/BF01582221

Coleman, T. F., & Li, Y. (1996). An interior, trust region approach for nonlinear minimization subject to bounds. *SIAM Journal on Optimization*, *6*, 418–445.

Crawford, W., Ballu, V., Bertin, X., & Karpytchev, M. (2015). The sources of deep ocean infragravity waves observed in the North Atlantic Ocean. *Journal of Geophysical Research: Oceans*, *120*, 5120–5133. https://doi.org/10.1002/2014JC010657

Dijkstra, E. W. (1959). A note on two problems in connexion with graphs. *Numerische Mathematik*, *1*(1), 269–271. https://doi.org/10.1007/BF01386390

Dumont, D., Kohout, A., & Bertino, L. (2011). A wave-based model for the marginal ice zone including a floe breaking parameterization. *Journal of Geophysical Research*, *116*, C04001. https://doi.org/10.1029/2010JC006682

Engwirda, D. (2017). JIGSAW-GEO (1.0): Locally orthogonal staggered unstructured grid generation for general circulation modelling on the sphere. *Geoscientific Model Development*, *10*(6), 2117–2140. https://doi.org/10.5194/gmd-10-2117-2017

Fox, C., & Squire, V. (1994). On the oblique reflexion and transmission of ocean waves at shore fast sea ice. *Philosophical Transactions: Physical Sciences and Engineering*, *347*(1682), 185–218.
Fox, C., & Squire, V. A. (1990). Reflection and transmission characteristics at the edge of shore fast sea ice. *Journal of Geophysical Research*, *95*(C7), 11,629–11,639. https://doi.org/10.1029/JC095iC07p11629
Godin, O. A., Zabotin, N. A., & Bullett, T. W. (2015). Acoustic-gravity waves in the atmosphere generated by infragravity waves in the ocean. *Earth, Planets and Space*, *67*(1), 47. https://doi.org/10.1186/s40623-015-0212-4
Godin, O. A., Zabotin, N. A., Sheehan, A. F., Yang, Z., & Collins, J. A. (2013). Power spectra of infragravity waves in a deep ocean. *Geophysical Research Letters*, *40*, 2159–2165. https://doi.org/10.1002/grl.50418
Gu, Y. J., & Sacchi, M. (2009). Radon Transform Methods and Their Applications in Mapping Mantle Reflectivity Structure. *Surveys in Geophysics*, *30*(4-5), 327–354. https://doi.org/10.1007/s10712-009-9076-0
Harmon, N., Henstock, T., Srokosz, M., Tilmann, F., Rietbrock, A., & Barton, P. (2012). Infragravity wave source regions determined from ambient noise correlation. *Geophysical Research Letters*, *39*, L04604. https://doi.org/10.1029/2011GL050414
Herbers, T. H. C., Elgar, S., & Guza, R. T. (1994). Infragravity-frequency (0.005-0.05 Hz) motions on the shelf, part I, forced waves. *Journal of Physical Oceanography*, *24*(5), 917–927. https://doi.org/10.1175/1520-0485(1994)024<0917:IFHMOT>2.0.CO;2
Herbers, T. H. C., Elgar, S., & Guza, R. T. (1995). Generation and propagation of infragravity waves. *Journal of Geophysical Research*, *100*(C12), 24,863–24,872. https://doi.org/10.1029/95JC02680
Herbers, T. H. C., Elgar, S., Guza, R. T., & O'Reilly, W. C. (1995). Infragravity-frequency (0.005-0.05 Hz) motions on the shelf. Part II: Free waves. *Journal of Physical Oceanography*, *25*(6), 1063–1079. https://doi.org/10.1175/1520-0485(1995)025
Ishii, M., Shearer, P. M., Houston, H., & Vidale J. E. (2005). Extent, duration and speed of the 2004 Sumatra–Andaman earthquake imaged by the Hi-Net array. *Nature*, *435*(7044), 933–936. https://doi.org/10.1038/nature03675
Kiser, E., & Ishii, M. (2017). Back-projection imaging of earthquakes. *Annual Review of Earth and Planetary Sciences*, *45*(1), 271–299. https://doi.org/10.1146/annurev-earth-063016-015801
Kohout, A. L., Williams, M. J. M., Dean, S. M., & Meylan, M. H. (2014). Storm-induced sea-ice breakup and the implications for ice extent. *Nature*, *509*(7502), 604–607. https://doi.org/10.1038/nature13262
Mahoney, A. R., Dammann, D. O., Johnson, M. A., Eicken, H., & Meyer, F. J. (2016). Measurement and imaging of infragravity waves in sea ice using InSAR. *Geophysical Research Letters*, *43*, 6383–6392. https://doi.org/10.1002/2016GL069583
Moore, E. H. (1920). On the reciprocal of the general algebraic matrix. *Bulletin of the American Mathematical Society*, *26*(9), 385–397. https://doi.org/10.1090/S0002-9904-1920-03322-7
Moser, T. J. (1991). Shortest path calculation of seismic rays. *Geophysics*, *56*(1), 59–67. https://doi.org/10.1190/1.1442958
Munk, W., Snodgrass, F., & Gilbert, F. (1964). Long waves on the continental shelf: An experiment to separate trapped and leaky modes. *Journal of Fluid Mechanics*, *20*(4), 529–554. https://doi.org/10.1017/S0022112064001392
Munk, W. H. (1949). Surf beats. *AGU Transactions*, *30*(6), 849–854. https://doi.org/10.1029/TR030i006p00849
Neale, J., Harmon, N., & Srokosz, M. (2015). Source regions and reflection of infragravity waves offshore of the USA's Pacific Northwest. *Journal of Geophysical Research: Oceans*, *120*, 6474–6491. https://doi.org/10.1002/2015JC010891
Okihiro, M., & Guza, R. T. (1996). Observations of Seiche forcing and amplification in three small harbors. *Journal of Waterway, Port, Coastal, and Ocean Engineering*, *122*(5), 232–238. https://doi.org/10.1061/(ASCE)0733-950X(1996)122:5(232)
Penrose, R. (1955). A generalized inverse for matrices. *Proceedings of the Cambridge Philosophical Society*, *51*(3), 406–413. https://doi.org/10.1017/S0305004100030401
Reniers, A. J. H. M., Groenewegen, M. J., Ewans, K. C., Masterton, S., Stelling, G. S., & Meek, J. (2010). Estimation of infragravity waves at intermediate water depth. *Coastal Engineering*, *57*(1), 52–61. https://doi.org/10.1016/J.COASTALENG.2009.09.013
Rhie, J., & Romanowicz, B. (2006). A study of the relation between ocean storms and the Earth's hum. *Geochemistry, Geophysics, Geosystems*, *7*, Q10004. https://doi.org/10.1029/2006GC001274
Ringdal, F., Husebye, E. S., & Dahle, A. (1975). P-wave envelope representation in event detection using array data. In K. G. Beauchamp (Ed.), *Exploitation of seismograph networks* (pp. 353–372). The Netherlands: Noordhoff-Leiden.
Sheremet, A., Staples, T., Ardhuin, F., Suanez, S., & Fichaut, B. (2014). Observations of large infragravity wave runup at Banneg Island, France. *Geophysical Research Letters*, *41*, 976–982. https://doi.org/10.1002/2013GL058880
Smit, P. B., Janssen, T. T., Herbers, T. H. C., Tiara, T., & Romanowicz, B. A. (2018). Infragravity wave radiation across the shelf break. *Journal of Geophysical Research: Oceans*, *123*, 4483–4490. https://doi.org/10.1029/2018JC013986
Squire, V., Vaughan, G. L., & Bennetts, L. G. (2009). Ocean surface wave evolvement in the Arctic Basin. *Geophysical Research Letters*, *36*, L22502. https://doi.org/10.1029/2009GL040676
Squire, V. A. (2007). Of ocean waves and sea-ice revisited, cold reg. *Science and Technology*, *49*(2), 110–133. https://doi.org/10.1016/j.coldregions.2007.04.007
Symonds, G., Huntley, D. A., & Bowen, A. J. (1982). Two-dimensional surf beat: Long wave generation by a time-varying breakpoint. *Journal of Geophysical Research*, *87*(C1), 492–498. https://doi.org/10.1029/JC087iC01p00492
Tonegawa, T., Fukao, Y., Shiobara, H., Sugioka, H., Ito, A., & Yamashita, M. (2018). Excitation location and seasonal variation of transoceanic infragravity waves ob-served at an absolute pressure gauge array. *Journal of Geophysical Research: Oceans*, *123*, 40–52. https://doi.org/10.1002/2017JC013488
Tucker, M. (1950). Surf beats: Sea waves of 1 to 5 min. period. *Proceedings of the Royal Society of London, Series A*, *202*, 565–573.
Uchiyama, Y., & McWilliams, J. C. (2008). Infragravity waves in the deep ocean: Generation, propagation, and seismic hum excitation. *Journal of Geophysical Research*, *113*, C07029. https://doi.org/10.1029/2007JC004562
Valentine, A. P., & Woodhouse, J. H. (2010). Approaches to automated data selection for global seismic tomography. *Geophysical Journal International*, *182*(2), 1001–1012. https://doi.org/10.1111/j.1365-246X.2010.04658.x
Wadhams, P., & Doble, M. J. (2009). Sea ice thickness measurement using episodic infragravity waves from distant storms. *Cold Regions Science and Technology*, *56*(2-3), 98–101. https://doi.org/10.1016/j.coldregions.2008.12.002
Webb, S. C. (2007). The Earth's hum is driven by ocean waves over the continental shelves. *Nature*, *445*(7129), 754–756. https://doi.org/10.1038/nature05536
Webb, S. C. (2008). The Earth's hum: The excitation of Earth normal modes by ocean waves. *Geophysical Journal International*, *174*(2), 542–566. https://doi.org/10.1111/j.1365-246X.2008.03801.x
Webb, S. C., Zhang, X., & Crawford, W. (1991). Infragravity waves in the deep ocean. *Journal of Geophysical Research*, *96*(C2), 2723–2736. https://doi.org/10.1029/90JC02212
Zabotin, N. A., Godin, O. A., & Bullett, T. W. (2016). Oceans are a major source of waves in the thermosphere. *Journal of Geophysical Research: Space Physics*, *121*, 3452–3463. https://doi.org/10.1002/2016JA022357